NANO LETTERS

pubs.acs.org/NanoLett Letter

Waveguide-Integrated $PdSe_2$ Photodetector over a Broad Infrared Wavelength Range

Jianghong Wu,[#] Hui Ma,[#] Chuyu Zhong,[#] Maoliang Wei, Chunlei Sun, Yuting Ye, Yan Xu, Bo Tang, Ye Luo, Boshu Sun, Jialing Jian, Hao Dai, Hongtao Lin,[*] and Lan Li[*]

Cite This: https://doi.org/10.1021/acs.nanolett.2c02099 Read Online

ACCESS | Metrics & More | Article Recommendations | Supporting Information

ABSTRACT: Hybrid integration of van der Waals materials on a photonic platform enables diverse exploration of novel active functions and significant improvement in device performance for next-generation integrated photonic circuits, but developing waveguide-integrated photodetectors based on conventionally investigated transition metal dichalcogenide materials at the full optical telecommunication bands and mid-infrared range is still a challenge. Here, we integrate $PdSe_2$ with silicon waveguide for on-chip photodetection with a high responsivity from 1260 to 1565 nm, a low noise-equivalent power of 4.0 $pW{\cdot}Hz^{-0.5}$, a 3-dB bandwidth of 1.5 GHz, and a measured data rate of 2.5 $Gbit{\cdot}s^{-1}$. The achieved $PdSe_2$ photodetectors provide new insights to explore the integration of novel van der Waals materials with integrated photonic platforms and exhibit great potential for diverse applications over a broad infrared range of wavelengths, such as on-chip sensing and spectroscopy.

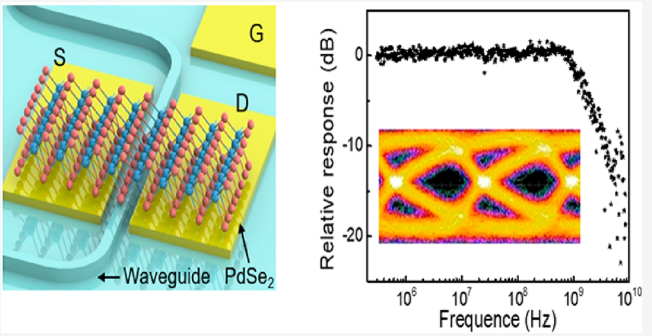

KEYWORDS: *Waveguide-integrated photodetector, $PdSe_2$, van der Waals materials, Integrated photonics, Infrared*

Integrated photonics has been a promising technology widely used in data communications and has gradually established a range of emerging applications in the area of sensing,[1] spectrometer,[2] light detection and ranging (LiDAR),[3] biological research,[4] and artificial skins.[5] To meet the functional requirements of various applications, integrated photonic systems consisting of multiple materials, including silicon,[6] III−V semiconductors,[7] lithium niobate,[8] silicon nitride,[9] polymers,[10] and amorphous glass,[11] have been proposed and developed. As one of the essential components in an integrated photonic circuit, the waveguide-integrated photodetector, converting the signal from photons to electrons, is usually constructed by integrating extrinsic materials on an integrated photonic platform. Currently, monolithic integration of germanium films on silicon is the most common strategy for waveguide-integrated photodetectors, but the threading dislocations and surface roughness at the interface are inevitable as the result of the 4.2% lattice mismatch between silicon and germanium, which need to be optimized by complex procedures. Furthermore, the demanding requirements for epitaxial growth make it difficult to integrate germanium with other photonic platforms based on silicon nitride, polymer, and amorphous glass. In contrast, van der Waals materials (VDWMs) are compatible with arbitrary substrates, overcoming the integration limitation induced by the variation of lattice constants and thermal expansion coefficients of each material platform.

Over the past decades, VDWMs have demonstrated intriguing optoelectronic properties, including ultrafast mobility, broadband absorption, and a dangling-bond-free surface, exhibiting great potential for optoelectronic devices.[12−18] Currently, integrating VDWMs with various integrated photonic platforms has already been realized, and a plethora of prototypical waveguide-integrated photodetectors have been developed.[19−24] Among all VDWMs, graphene has been extensively studied for waveguide-integrated photodetectors, but graphene photodetectors suffer from a large dark current because of a zero bandgap. Although graphene photodetectors based on photothermoelectric effect (PTE) can work without bias voltage, they usually need a complex device structure such as local doping to obtain the different Seebeck coefficients.[19] VDW semiconductors such as black phosphorus (BP), $MoTe_2$ and Bi_2O_2Se are alternative candidates.[25−28] However, the air-unstability of BP limits the applications, and a large optical bandgap for $MoTe_2$ (1.04 eV) and Bi_2O_2Se (0.9 eV) prevents them from optical detection at the C-band and mid-infrared (MIR) region.

Received: May 25, 2022
Revised: June 29, 2022

https://doi.org/10.1021/acs.nanolett.2c02099
Nano Lett. XXXX, XXX, XXX−XXX

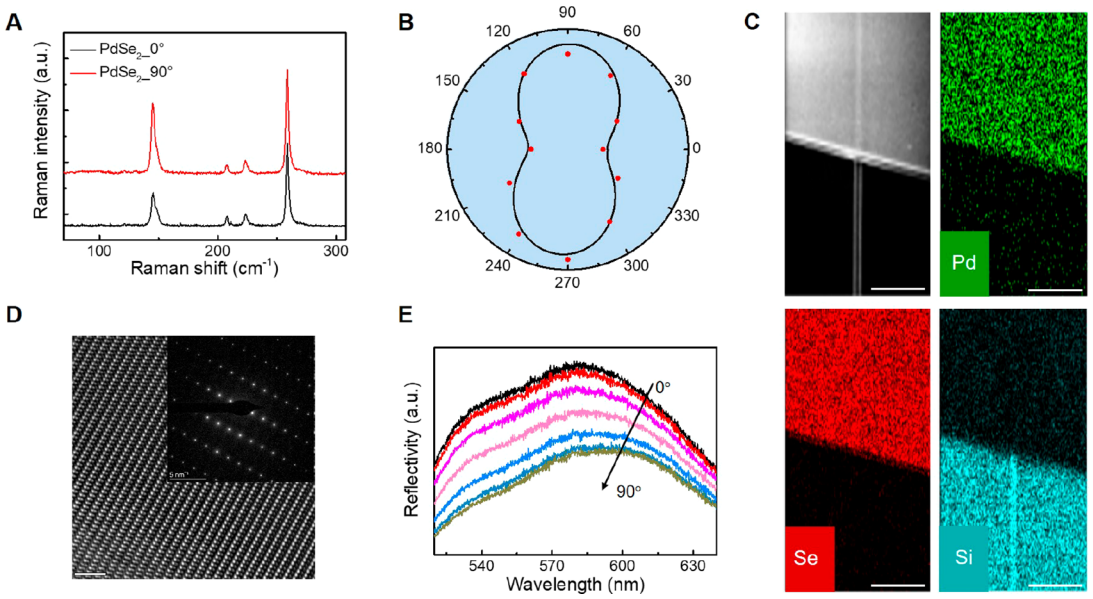

Figure 1. Multilayer $PdSe_2$ flake characterization. (A) Raman spectra of a multilayer $PdSe_2$ excited by incident light at 532 nm under two different polarization states. (B) Polar plots of the measured and fitted peak intensities of the A_g^1 mode. (C) The energy-dispersive X-ray spectroscopy (EDS) mappings of a multilayer $PdSe_2$ flake on an SOI ridge waveguide. Scale bar: 5 μm. (D) High-resolution transmission electron microscope (TEM) image of a multilayer $PdSe_2$ film. The illustration is the corresponding selected area electron diffraction (SAED) pattern. Scale bar: 2 nm. (E) Reflection spectra of a multilayer $PdSe_2$ flake with a white light source under different polarization states.

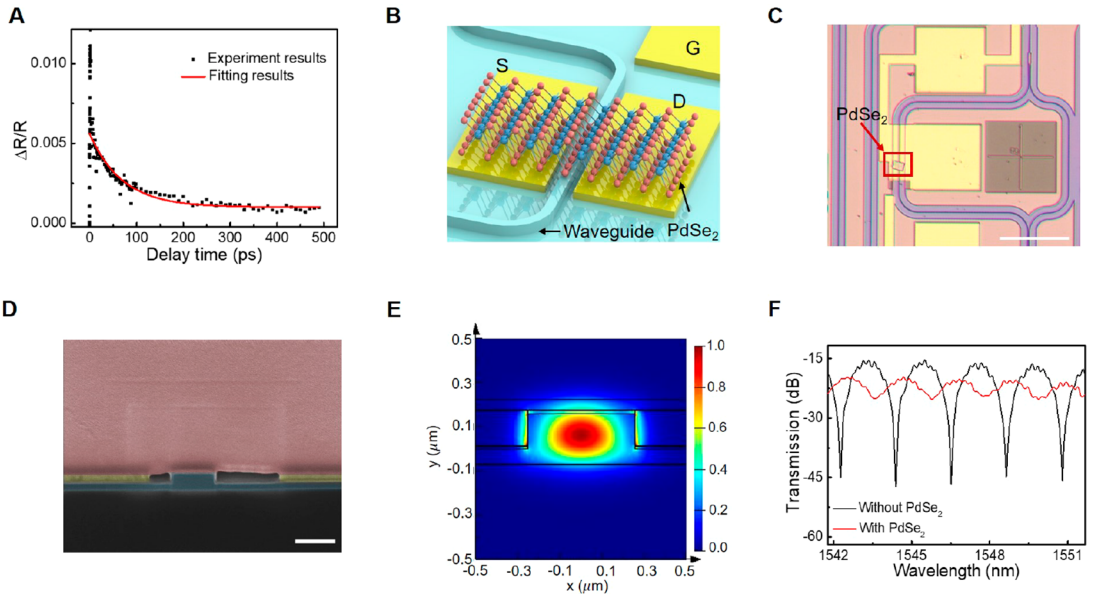

Figure 2. $PdSe_2$ photodetector integrated with a silicon photonic circuit. (A) Measured ultrafast transient reflectance of a multilayer $PdSe_2$ flake (12 nm thick). (B) Three-dimensional illustration of the waveguide-integrated $PdSe_2$ photodetector. (C) Optical image of a $PdSe_2$ waveguide-integrated photodetector. Scale bar: 100 μm. (D) Cross-section scanning electron microscope (SEM) image of a $PdSe_2$ photodetector. Bule region is Si waveguide, brown region is $PdSe_2$, yellow region is Au electrode. Scale bar: 500 nm. (E) Calculated electric field profiles of the TE_0 mode in the hybrid silicon/$PdSe_2$ waveguide; the thickness of the $PdSe_2$ flake is 50 nm. (F) Transmission spectra of the unbalanced MZI with and without a $PdSe_2$ flake (155 nm thick).

Recently, $PdSe_2$ with great air-stability and a large bandgap tunability, ranging from 0.03 eV (bulk) to ~1.3 eV (monolayer) has been a new candidate for optoelectronic applications at NIR and MIR.[29−32] Moreover, a wafer-scale $PdSe_2$ can be obtained by a simple selenization process of the predeposited Pd film,[33,34] and a centimeter-scale $PdSe_2$ can be prepared by chemical vapor deposition method,[35] which ensures the fabrication of a device array. To date, free-space $PdSe_2$ photodetectors have already been investigated. For example, a $PdSe_2$ phototransistor showed photoresponse ranging from the visible to MIR with a slow response time.[36] The VDW heterostructure, such as InSe/$PdSe_2$ and $PdSe_2$/MoS_2 showed photoresponse at NIR and MIR, but the rise/fall times were tens of milliseconds.[37,38] Up to now, realizing a $PdSe_2$ photodetector with high responsivity and large bandwidth is still a challenge and highly desired. Indeed, a waveguide architecture is attractive for designing photodetectors with both high responsivity and large bandwidth. It

https://doi.org/10.1021/acs.nanolett.2c02099
Nano Lett. XXXX, XXX, XXX−XXX

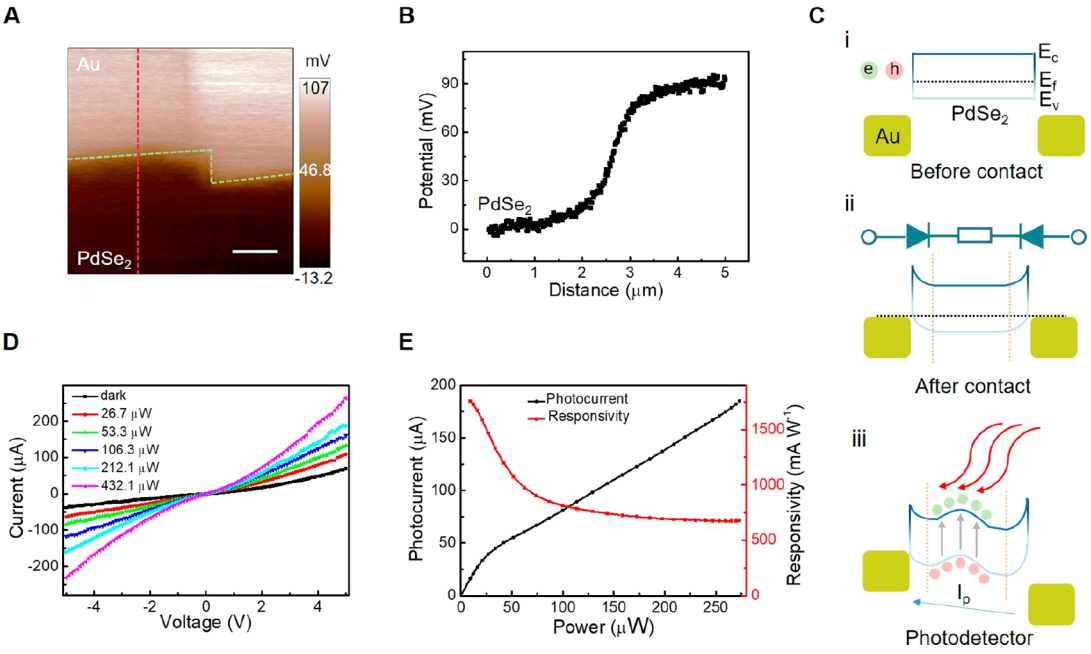

Figure 3. Electronic characteristics of $PdSe_2$ photodetector. (A) Kelvin probe force microscopy (KPFM) image of the Au-$PdSe_2$ contact on a Si/SiO_2 substrate, where the green dot line is the edge of the $PdSe_2$ flake and Au electrode. Scale bar: 1 μm. (B) KPFM profile along with the red dashed line in part A. (C) Energy band diagram of Au-$PdSe_2$−Au junction at equilibrium, under illumination, at a bias voltage, and corresponding equivalent circuits. (D) Current−voltage (IV) curves a waveguide-integrated $PdSe_2$ photodetector (Sample 1, S1) in the dark and under illumination with different optical power at 1550 nm. (E) Photocurrent and responsivity versus incident optical power at 5 V.

can simultaneously ensure adequate absorption via evanescent field coupling over a long propagation distance and decrease the transit time of photoinduced carriers with a short channel.

In this work, we proposed and demonstrated waveguide-integrated $PdSe_2$ photodetectors operating in the telecom optical bands ranging from the O-band to the C-band. The significant optoelectronic properties of multilayer $PdSe_2$, including anisotropy and ultrafast carrier dynamics, were characterized. We integrated silicon-on-insulator (SOI) ridge waveguides with the multilayer $PdSe_2$ which were exfoliated from bulk materials and transferred by an imprint-transfer process. Such devices ensure sufficient optical absorption for the fundamental mode of TE polarization (TE_0). The present $PdSe_2$ waveguide-integrated photodetectors possess a broadband spectral operation, a high responsivity of 1758.7 mA·W^{-1}, and a low noise-equivalent power (NEP) of 4.0 pW·$Hz^{-0.5}$ at 1550 nm (5 V). Additionally, a 3-dB bandwidth reaches up to 1.5 GHz, and the eye diagram indicates $PdSe_2$ photodetector could realize a data transmission rate being more than 2.5 Gbit·s^{-1}.

Raman spectra of a multilayer $PdSe_2$ flake on SiO_2 substrate are shown in Figure 1A, where four distinct Raman peaks at about 143, 206, 222, and 256 cm^{-1} are observed, which are corresponding to A_g^1, A_g^2, B_{1g}^2, and A_g^3 modes, respectively. Furthermore, the measured Raman spectra under different polarization states show the strong in-plane anisotropic phonon vibration (Figure S1A). The polarization-dependent Raman intensity of A_g^1−B_{1g}^1 (Figure 1B) shows clear periodical variations of π. The chemical composition of multilayer $PdSe_2$ was characterized by X-ray photoelectron spectroscopy (XPS) measurement (Figure S1) in which four typical peaks at 54.6, 55.4, 336.7, and 342.1 eV are ascribed to Se $3d_{5/2}$, $3d_{3/2}$, Pd $3d_{5/2}$, and $3d_{3/2}$ orbitals, respectively. The EDS mappings of a multilayer $PdSe_2$ flake on an SOI ridge waveguide are shown in Figure 1C, where Pd and Se elements show a uniform distribution. Moreover, the high-magnification TEM image and SAED pattern in Figure 1D demonstrate the single-crystal characteristic of the exfoliated multilayer $PdSe_2$ flake. Additionally, anisotropic optical properties were confirmed by the variation of the reflection spectra under different polarization states (Figure 1E), and the reflectivity decreases gradually when the polarization angle increases from 0° to 90°, which indicates that the crystal orientation has an impact on photon-to-electron transition.

The lifetime of photoinduced carriers was inferred by the ultrafast transient reflectance (TR) spectroscopy. We excited a multilayer $PdSe_2$ flake with a 2.07 eV pump pulse (50 fs pulse duration) and measured the reflectance change using a white-light continuum probe. The TR kinetics (Figure 2A) indicates that the lifetime of photoinduced carriers of this $PdSe_2$ flake (12 nm thick in Figure S1D) is about 68 ps. With the thickness increase, a narrowing bandgap induces a shorter lifetime of photoinduced carriers, and the measured lifetime under 1550 nm wavelength illumination is 22 ps for a multilayer $PdSe_2$ flake (20 nm thick) in the previous report.[39] The lifetime is longer than that counterpart of graphene,[40] indicating $PdSe_2$ photodetectors can not only realize a high photoconductive gain ($G = \tau_{life}/\tau_{tran}$, τ_{tran} is the drift transit time), but also a large 3-dB bandwidth.

Figure 2B shows the schematic configuration, where SOI ridge waveguide (220 nm thick) with an etching height of 150 nm is applied. The silicon waveguide was lightly doped, and the heavily doped area (2×10^{20} cm^{-3}) was close to the waveguide at a suitable distance. The Al_2O_3 film (15 nm thick) was deposited to avoid photoinduced carriers transferring between a $PdSe_2$ flake and the Si waveguide. Two Ti/Au pads (5/100 nm) were deposited and placed around the straight waveguide, and a $PdSe_2$ flake was transferred to the top of a

https://doi.org/10.1021/acs.nanolett.2c02099
Nano Lett. XXXX, XXX, XXX−XXX

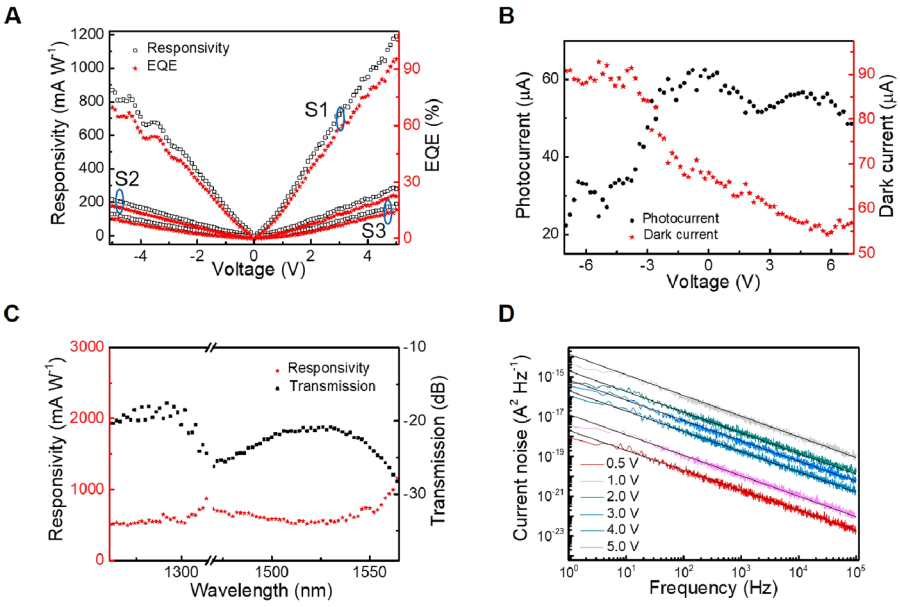

Figure 4. Static performance of $PdSe_2$ photodetectors. (A) Responsivity and EQE for S1, S2, and S3 at different bias voltage under the illumination of 1550 nm. (B) Gate-tunable transport and photoresponse of a $PdSe_2$ photodetector (S1), the optical power is 42 μW). (C) Spectral response of $PdSe_2$ photodetectors (the measured results at O-band are obtained by S4, and others are obtained by S1). (D) $1/f$ noise spectra of a waveguide-integrated $PdSe_2$ photodetector (S1) under different applied voltages. The black lines show the best fitting of the test results.

waveguide. Incident light was coupled into/out waveguide by two grating couplers whose SEM images are illustrated in Figure S2. The detailed process of device fabrication is shown in Supporting Information. A typical optical image of the waveguide-integrated $PdSe_2$ photodetector is shown in Figure 2C, where a $PdSe_2$ flake is on one arm of an unbalanced Mach−Zehnder interferometer (MZI). The cross-section SEM image of a waveguide-integrated $PdSe_2$ photodetector (Figure 2D) indicates that an altitude difference remains at the top of the waveguide core, slab and Au pads, and a part of the $PdSe_2$ flake is suspended. The adhesion between a $PdSe_2$ flake and the waveguide substrate was strong enough, which has been verified in subsequent experiments.

The simulated electric field profile of the TE_0 mode indicates that $PdSe_2$ can not only realize optical absorption at 1550 nm but also avoid a high mode-mismatching loss (Figure 2E). The experimental optical absorption was characterized by comparing the transmission spectra of an unbalanced MZI (Figure 2F) with/without a $PdSe_2$ flake. In this unbalanced MZI, beam splitter and combiner are realized by two 1 × 2 MMIs. The detailed performance of a 1 × 2 MMI (Figure S3) indicates that it splits incident light power equally. According to the change of extinction ratio (ER), the absorption coefficient of the $PdSe_2$ (155 nm thick)/Si hybrid waveguide is calculated to be 0.14 dB/μm at 1550 nm. We also demonstrated the transmission spectra variation of a straight waveguide with/without a $PdSe_2$ flake (Figure S9A). Actually, the slight difference in grating couplers during different operations leads to an experimental error in the absorption coefficient of the $PdSe_2$/Si hybrid waveguide, which could be avoided by measuring from an MZI.

Next, we measured the contact potential difference (V_{CPD}) between an Au electrode and a $PdSe_2$ flake by KPFM. The KPFM image of a $PdSe_2$−Au junction (Figure 3A) indicates the different work functions for an Au electrode and a $PdSe_2$ flake, and the detailed surface potential profile along the red dot line (Figure 3B) shows that the work function difference is about 90 meV. The smaller work function results in electron transferring from $PdSe_2$ flake to Au electrode, with an upward sloping of the energy band, and a built-in electric field at the contact interface. Therefore, the equivalent circuit can be regarded as a back-to-back Schottky junction (Figure 3C). The photovoltaic effect (PVE) is usually dominant for free-space photodetectors based on Au−semiconductor−Au structure. However, the optical absorption of a $PdSe_2$ flake is mainly located on top of a waveguide surface (Figure 2E), and the distance between the Au electrode and optical absorption area is larger than the width of the depletion area. Thereby, photocurrent at 0 V is extremely weak in this photodetector, similar to waveguide-integrated photodetector based on BP.[27] Moreover, the weak photocurrent at 0 V excludes PTE effect as well. Additionally, photobolometric effect is also eliminated because the photocurrent increases nonlinearly with the bias voltage.[41]

The static characteristics of a $PdSe_2$ photodetector (sample1) were measured, and IV curves in the dark and under illumination at 1550 nm were demonstrated (Figure 3D). The nonlinear property of IV curves is attributed to a Schottky barrier at the contact interface between Au and $PdSe_2$, which is primarily attributed to two aspects. On the one hand, a low background doping level of the multilayer $PdSe_2$ flake[42] brings about a large depletion layer width. On the other hand, a multilayer $PdSe_2$ flake was transferred onto the Au electrode, avoiding unnecessary chemical disorder and Fermi-level pinning, leading to a better Schottky junction.[43] The dark current is −38 μA at −5 V, with the $PdSe_2$ thickness of 139 nm (Figure S5), which decreases with the thinner thickness.[44] Furthermore, aligning the crystal orientation has an impact on dark current,[45] approved by the anisotropic electronic transport (Figure S6), which provides flexibility to the device design. The photocurrent-incident optical power curve (Figure 3E) at 5 V shows the nonlinear property at the small optical power, which is primarily attributed to the low-lying, long-lived traps in $PdSe_2$. In the future, a larger linear dynamic range can

https://doi.org/10.1021/acs.nanolett.2c02099
Nano Lett. XXXX, XXX, XXX−XXX

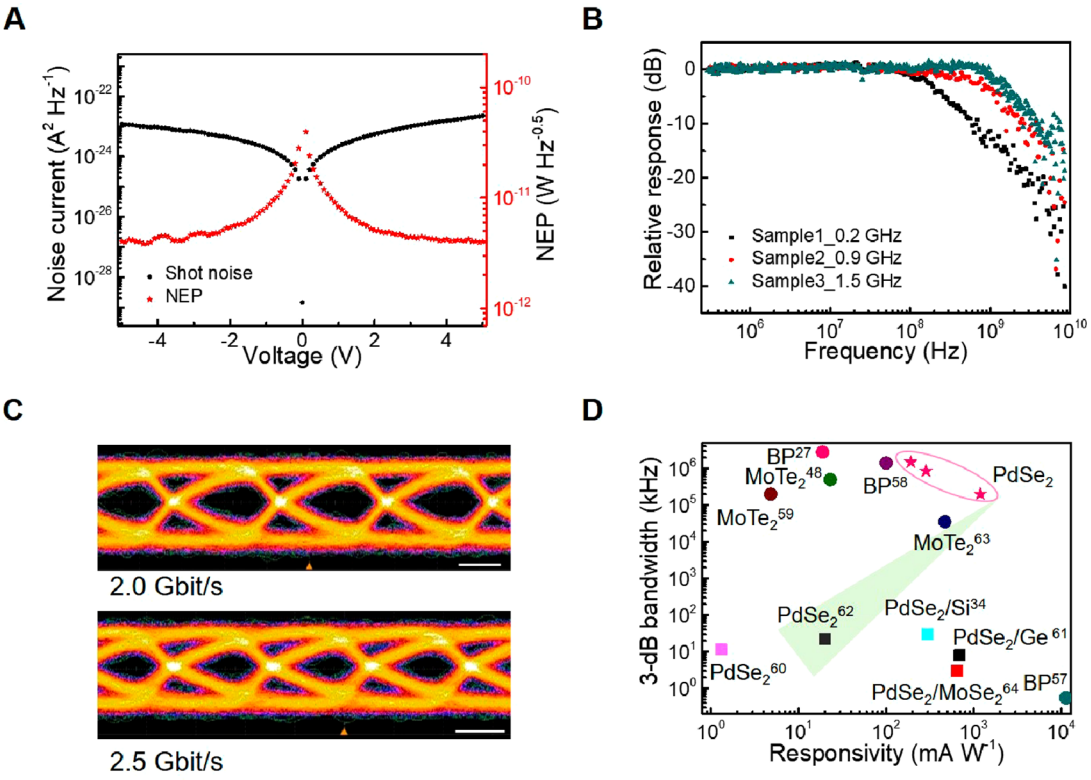

Figure 5. Dynamic performance of $PdSe_2$ photodetectors. (A) NEP and noise current induced by shot noise at different bias voltage. (B) Measured frequency response of three $PdSe_2$ photodetectors (S1, S2 and S3) at 3 V. (C) Receiver eye diagram at a data rate of 2.0 and 2.5 Gbit s^{-1} measured with a $PdSe_2$ photodetector (S3). Scale bar: 200 ps. (D) Summary of the performance for waveguide-integrated photodetectors (circular shapes) based on VDW semiconductors and free-space photodetectors (rectangular shapes) based on $PdSe_2$ flakes. Three five-pointed stars represent waveguide-integrated photodetectors (S1, S2, and S3). The green arrow indicates the direction of device with improved performance.

be obtained by growing the high-quality $PdSe_2$ without trap states.

Responsivity varies as a function of bias voltage (Figure 4A) because the higher efficiency of the generation-separation-collection process of photoinduced carriers can be realized at a larger bias voltage. The external responsivity ($R = I_p/P_{in}$) is 1190.2, 285.7, and 191.2 mA·W^{-1} at 5 V and 1550 nm for S1, S2, and S3, respectively, and the external quantum efficiency (EQE = 1.24 × R/λ) is 95.2%, 22.9%, and 15.3%, where λ is the incident light wavelength. Such an external responsivity and EQE are higher than the counterparts based on graphene,[46,47] BP,[27] and $MoTe_2$.[48] The variation of responsivities for these three samples (S1, S2, and S3) is mainly attributed to the thickness, length, and optical anisotropy of the multilayer $PdSe_2$ flakes. The exact sizes of $PdSe_2$ are listed in Table S1. Moreover, the reflectivity varies under different polarization states (Figure 1E), illustrating that optical anisotropy has a severe impact on the optical absorption and the photo-to-electron transition, which is consistent with previous reports.[49,50] Additionally, responsivity is affected by different $PdSe_2$ thicknesses (Figure S7). When the $PdSe_2$ thickness is less than 5.3 nm, the photon-to-electron transition limited by a large optical bandgap is extremely weak, and the $PdSe_2$ thickness is expected to be thicker than 11.8 nm for efficient optical absorption at 1550 nm.

I_d−V_g curve (Figure 4B) in the dark shows a small on−off ratio for a $PdSe_2$ photodetector (S1), indicating the $PdSe_2$ flake is p-doped, which is consistent with previous reports.[42] The thickness of the $PdSe_2$ flake (139 nm thick) is significantly greater than the Debye screening length, resulting in the device not being thoroughly turned off and a moderate gate-dependent transport. Another two $PdSe_2$ field-effect transistors on a SiO_2/Si substrate also verify the gate-dependent transport (Figure S8). The transport indicates that multilayer $PdSe_2$ flake possesses a low background doping because the onset of different doping locates about V_g = 0 V. Moreover, the gate-dependent photocurrent is primarily attributed to the variation of optical absorption of $PdSe_2$ flakes (Figure 4B), rather than the larger thermionic and tunneling currents,[51] being similar to graphene photodetectors.[52] As shown in Figure 2D, carrier variation induced by a back-gate voltage mainly concentrates on the area at the top surface of a waveguide; thereby, a back-gate voltage has little impact on the $PdSe_2$−Au Schottky barriers, as well as thermionic and tunneling currents. Similar results, including the unipolar dark current and maximal photocurrent at V_g = 0 V were observed in another waveguide-integrated photodetector as well (Figure S9).

The spectral photoresponse (Figure 4C) demonstrates the broadband operation of $PdSe_2$ photodetectors, and the responsivity is more than 500 mA·W^{-1} with input optical power being larger than 200 μW at 5 V. Limited by a finite optical bandwidth of grating couplers, we fabricated two photodetectors (S1 and S4) to show this broadband spectral photoresponse. One photodetector (S4) works at O-band, corresponding to the responsivity at wavelengths from 1260 to 1325 nm, and the detailed characteristics of S4 are illustrated (Figure S10). Another photodetector (S1) works at wavelengths from 1470 to 1565 nm. The fluctuating responsivity is attributed to the incident power variation at different wavelengths. During this measurement, since the output

https://doi.org/10.1021/acs.nanolett.2c02099
Nano Lett. XXXX, XXX, XXX−XXX

power of the laser at different wavelengths was fixed, the practical incident power passing through the waveguide at different wavelengths was different due to various coupling efficiencies of the grating couplers. A smaller incident power usually brings about a large photocurrent gain and responsivity; thereby, the responsivity at the wavelengths with a weak coupling efficiency is higher, which is consistent with the measured result in Figure 3E. Furthermore, the operational wavelengths of $PdSe_2$ photodetectors can be extended to MIR as well. The photocurrent of free-space $PdSe_2$ photodetectors with illumination at 2 μm can be observed in Figure S4.

Moreover, we analyzed the noise-equivalent power (NEP = i_n/R) of the $PdSe_2$ photodetectors, where i_n is the noise current. The measured $1/f$ noise spectral density in Figure 4D indicates that $PdSe_2$ photodetectors possess typical characteristics of $1/f$ noise, which can be determined by the Hooge's empirical relationship ($S_i = A{\cdot}i^{\alpha}/f^{\beta}$),[53,54] where i, f, and A are the channel current, the frequency, and the noise amplitude, respectively. β is fitted to be 1.0, 1.03, 1.02, 1.02, 1.04, and 1.04 for bias voltages at 0.5, 1.0, 2.0, 3.0, 4.0, and 5.0 V. Moreover, the current noise induced by the shot noise and the thermal noise are evaluated to be 2.24×10^{-23} and 2.32×10^{-25} $A^2{\cdot}Hz^{-1}$ at 5.0 V. Usually, the $1/f$ noise dominates at a small frequency,[54] but the measured $1/f$ noise is much larger than the shot noise at 10^5 Hz. The origin of such a high $1/f$ noise in the $PdSe_2$ photodetector probably results from the fluctuating occupancy of trap states which enlarges the fluctuation of carrier density, leading to the $1/f$-spectra extending over a higher frequency.[55] The remaining trap states in $PdSe_2$ are confirmed by the obvious photocurrent gain at low optical power. Assuming that β is an invariant constant when the $1/f$ noise is larger than the shot noise, the turning point of white noise is about 700 MHz, and NEP is estimated to be 4.0 pW·$Hz^{-0.5}$ at 5 V. Furthermore, the current noise for a $PdSe_2$ photodetector increases with the applied voltage, but a smaller NEP is obtained at the larger bias voltage (Figure 5A). This phenomenon is attributed to the fact that a larger bias voltage brings about a higher efficiency of the separation-collection process of photogenerated carriers and a larger responsivity.

The measured 3-dB bandwidths for S1, S2, and S3 are about 0.2, 0.9, and 1.5 GHz, respectively (Figure 5B), whose measurement setup is shown in Figure S11. The total response time is determined by the carrier with a transit time (τ_{tr}) and the charge/discharge time of the junction capacitance (τ_{RC}). The τ_{tr} can be written as $\tau_{tr} = \frac{l^2}{2\mu V_{DS}}$, where l, μ, V_{DS} are the length of a $PdSe_2$ photodetector, the mobility of a $PdSe_2$ flake, and the bias voltage, respectively. Mobility of $PdSe_2$ was measured to be 216 $cm^2{\cdot}V^{-1}{\cdot}s^{-1}$,[56] the calculated τ_{tr} is about 29 ps (5.3 GHz) at 5 V. However, the measured 3-dB bandwidths remained almost at the same value for S3 (Figure S12), indicating that total response time (τ) is determined by τ_{RC}. Impedance matching in measurement is necessary for a $PdSe_2$ photodetector with larger bandwidth in the future. Additionally, we performed an eye-diagram measurement to illustrate the feasibility of $PdSe_2$ photodetectors for receiving high bit-rate data. The experimental results (Figure 5C) demonstrate a completely open eye at 3 V with a data rate of 2.5 Gbit·s^{-1}. Overall, the proposed $PdSe_2$ photodetectors show apparent advantages compared with photodetectors based on VDW semiconductors (Figure 5D),[27,34,48,57−64] and the detailed comparison is listed in Supporting Information.

In summary, we have realized integrated photodetectors based on SOI ridge waveguides and multilayer $PdSe_2$ covering the datacom and telecom wavelength range (1260−1565 nm). The obtained photodetectors possessed a high responsivity of 1758.7 mA·W^{-1} at 1550 nm, a 3-dB bandwidth of 1.5 GHz, a data rate being more than 2.5 Gbit·s^{-1}, and a NEP of about 4.0 pW·$Hz^{-0.5}$. In the future, the 3-dB bandwidth can be optimized by both reducing the contact resistance between $PdSe_2$ flakes and metal electrodes and shortening the channel length. Overall, these results pave the way for integrating $PdSe_2$ flake onto an integrated photonic platform and provide a new route to integrated photodetectors for applications in diverse areas, including optical communications, on-chip spectroscopy, and sensing.

■ ASSOCIATED CONTENT

Supporting Information

The Supporting Information is available free of charge at https://pubs.acs.org/doi/10.1021/acs.nanolett.2c02099.

Additional results and details for waveguide-integrated photodetector fabrication and measurement, multilayer $PdSe_2$ flakes characterization, SEM and performance of the passive integrated device, photoresponse of free-space $PdSe_2$ photodetector at 2 μm, AFM results for $PdSe_2$, characterization of the anisotropic electronic transport property, gate-dependent transport properties measurement, static photoresponse, dynamic measurement setups, and dynamic response of S3 under different bias voltages (PDF)

■ AUTHOR INFORMATION

Corresponding Authors

Lan Li − *Key Laboratory of 3D Micro/Nano Fabrication and Characterization of Zhejiang Province, School of Engineering, Westlake University, Hangzhou 310024, China; Institute of Advanced Technology, Westlake Institute for Advanced Study, Hangzhou 310024, China;* orcid.org/0000-0002-9097-9157; Email: lilan@westlake.edu.cn

Hongtao Lin − *State Key Laboratory of Modern Optical Instrumentation, College of Information Science and Electronic Engineering, Zhejiang University, Hangzhou 310027, China; MOE Frontier Science Center for Brain Science & Brain-Machine Integration, Zhejiang University, Hangzhou 310027, China;* orcid.org/0000-0001-7432-3644; Email: hometown@zju.edu.cn

Authors

Jianghong Wu − *State Key Laboratory of Modern Optical Instrumentation, College of Information Science and Electronic Engineering, Zhejiang University, Hangzhou 310027, China; Key Laboratory of 3D Micro/Nano Fabrication and Characterization of Zhejiang Province, School of Engineering, Westlake University, Hangzhou 310024, China; Institute of Advanced Technology, Westlake Institute for Advanced Study, Hangzhou 310024, China*

Hui Ma − *State Key Laboratory of Modern Optical Instrumentation, College of Information Science and Electronic Engineering, Zhejiang University, Hangzhou 310027, China; MOE Frontier Science Center for Brain Science & Brain-Machine Integration, Zhejiang University, Hangzhou 310027, China*

https://doi.org/10.1021/acs.nanolett.2c02099
Nano Lett. XXXX, XXX, XXX−XXX

Chuyu Zhong − *State Key Laboratory of Modern Optical Instrumentation, College of Information Science and Electronic Engineering, Zhejiang University, Hangzhou 310027, China; MOE Frontier Science Center for Brain Science & Brain-Machine Integration, Zhejiang University, Hangzhou 310027, China*

Maoliang Wei − *State Key Laboratory of Modern Optical Instrumentation, College of Information Science and Electronic Engineering, Zhejiang University, Hangzhou 310027, China; MOE Frontier Science Center for Brain Science & Brain-Machine Integration, Zhejiang University, Hangzhou 310027, China*

Chunlei Sun − *Key Laboratory of 3D Micro/Nano Fabrication and Characterization of Zhejiang Province, School of Engineering, Westlake University, Hangzhou 310024, China; Institute of Advanced Technology, Westlake Institute for Advanced Study, Hangzhou 310024, China*

Yuting Ye − *Key Laboratory of 3D Micro/Nano Fabrication and Characterization of Zhejiang Province, School of Engineering, Westlake University, Hangzhou 310024, China; Institute of Advanced Technology, Westlake Institute for Advanced Study, Hangzhou 310024, China*

Yan Xu − *Key Laboratory of 3D Micro/Nano Fabrication and Characterization of Zhejiang Province, School of Engineering, Westlake University, Hangzhou 310024, China; Institute of Advanced Technology, Westlake Institute for Advanced Study, Hangzhou 310024, China*

Bo Tang − *Institute of Microelectronics, Chinese Academic Society, Beijing 100029, China*

Ye Luo − *Key Laboratory of 3D Micro/Nano Fabrication and Characterization of Zhejiang Province, School of Engineering, Westlake University, Hangzhou 310024, China; Institute of Advanced Technology, Westlake Institute for Advanced Study, Hangzhou 310024, China*

Boshu Sun − *State Key Laboratory of Modern Optical Instrumentation, College of Information Science and Electronic Engineering, Zhejiang University, Hangzhou 310027, China; MOE Frontier Science Center for Brain Science & Brain-Machine Integration, Zhejiang University, Hangzhou 310027, China*

Jialing Jian − *Key Laboratory of 3D Micro/Nano Fabrication and Characterization of Zhejiang Province, School of Engineering, Westlake University, Hangzhou 310024, China; Institute of Advanced Technology, Westlake Institute for Advanced Study, Hangzhou 310024, China*

Hao Dai − *State Key Laboratory of Modern Optical Instrumentation, College of Information Science and Electronic Engineering, Zhejiang University, Hangzhou 310027, China; MOE Frontier Science Center for Brain Science & Brain-Machine Integration, Zhejiang University, Hangzhou 310027, China*

Complete contact information is available at: https://pubs.acs.org/10.1021/acs.nanolett.2c02099

Author Contributions

L.L, H.L., and J.W. conceived the project. J.W., H.M., C.Z., M.W., Y.Y., Y.X., B.T., Y.L., B.S., J.J., and H.D. fabricated these devices. J.W., M.W., and C.S. designed the passive optical devices. J.W. performed the optical and optoelectronic measurements. L.L, H.L., and J.W. analyzed the data and wrote the manuscript. All authors commented on the manuscript.

Author Contributions

[#]J.W., H.M., and C.Z. contributed equally to this work.

Notes

The authors declare no competing financial interest.

■ ACKNOWLEDGMENTS

The authors thank ZJU Micro-Nano Fabrication Center at Zhejiang University, Westlake Center for Micro/Nano Fabrication and Instrumentation and Service Center for Physical Sciences at Westlake University for the facility support, and Prof. Haiming Zhu and Mr. Cheng Sun for the support of ultrafast transient reflectance measurement. The research was partially supported by the National Key Research and Development Program of China (2019YFB2203003), National Natural Science Foundation of China (Grant Numbers 12104375, 62175202, 61975179 and 91950204), Leading Innovative and Entrepreneur Team Introduction Program of Zhejiang (2020R01005), Zhejiang Provincial Natural Science Foundation of China (LD22F040002) and the Foundation of Key Laboratory of 3D Micro/Nano Fabrication and Characterization of Zhejiang Province, Westlake University.

■ REFERENCES

(1) Chen, Y.; Lin, H.; Hu, J.; Li, M. Heterogeneously integrated silicon photonics for the mid-infrared and spectroscopic sensing. *ACS Nano* **2014**, *8*, 6955−6961.

(2) Le Coarer, E.; Blaize, S.; Benech, P.; Stefanon, I.; Morand, A.; Lérondel, G.; Leblond, G.; Kern, P.; Fedeli, J. M.; Royer, P. Wavelength-scale stationary-wave integrated Fourier-transform spectrometry. *Nat. Photonics* **2007**, *1*, 473−478.

(3) Zhang, X.; Kwon, K.; Henriksson, J.; Luo, J.; Wu, M. C. A large-scale microelectromechanical-systems-based silicon photonics LiDAR. *Nature* **2022**, *603*, 253−258.

(4) Mohanty, A.; Li, Q.; Tadayon, M. A.; Roberts, S. P.; Bhatt, G. R.; Shim, E.; Ji, X.; Cardenas, J.; Miller, S. A.; Kepecs, A.; et al. Reconfigurable nanophotonic silicon probes for sub-millisecond deep-brain optical stimulation. *Nat. Biomed. Eng.* **2020**, *4*, 223−231.

(5) Zhang, L.; Pan, J.; Zhang, Z.; Wu, H.; Yao, N.; Cai, D.; Xu, Y.; Zhang, J.; Sun, G.; Wang, L.; et al. Ultrasensitive skin-like wearable optical sensors based on glass micro/nanofibers. *Opto-Electron. Adv.* **2020**, *3*, 19002201−19002207.

(6) Soref, R. The past, present, and future of silicon photonics. *IEEE J. Sel. Top. Quantum Electron.* **2006**, *12*, 1678−1687.

(7) Roelkens, G.; Liu, L.; Liang, D.; Jones, R.; Fang, A.; Koch, B.; Bowers, J. III-V/silicon photonics for on-chip and intra-chip optical interconnects. *Laser Photonics Rev.* **2010**, *4*, 751−779.

(8) Zhu, D.; Shao, L.; Yu, M.; Cheng, R.; Desiatov, B.; Xin, C.; Hu, Y.; Holzgrafe, J.; Ghosh, S.; Shams-Ansari, A.; et al. Integrated photonics on thin-film lithium niobate. *Adv. Opt. Photonics* **2021**, *13*, 242−352.

(9) Liang, G.; Huang, H.; Mohanty, A.; Shin, M. C.; Ji, X.; Carter, M. J.; Shrestha, S.; Lipson, M.; Yu, N. Robust, efficient, micrometre-scale phase modulators at visible wavelengths. *Nat. Photonics* **2021**, *15*, 908−913.

(10) Dangel, R.; Hofrichter, J.; Horst, F.; Jubin, D.; La Porta, A.; Meier, N.; Soganci, I. M.; Weiss, J.; Offrein, B. J. Polymer waveguides for electro-optical integration in data centers and high-performance computers. *Opt. Express* **2015**, *23*, 4736−4750.

(11) Li, L.; Lin, H.; Qiao, S.; Huang, Y.-Z.; Li, J.-Y.; Michon, J.; Gu, T.; Alosno-Ramos, C.; Vivien, L.; Yadav, A.; et al. Monolithically integrated stretchable photonics. *Light-Sci. Appl.* **2018**, *7*, 17138−17138.

(12) Wu, J.; Ma, H.; Yin, P.; Ge, Y.; Zhang, Y.; Li, L.; Zhang, H.; Lin, H. Two-Dimensional Materials for Integrated Photonics: Recent Advances and Future Challenges. *Small Science* **2021**, *1*, 2000053.

(13) Rezaei, M.; Bianconi, S.; Lauhon, L. J.; Mohseni, H. A New Approach to Designing High-Sensitivity Low-Dimensional Photodetectors. *Nano Lett.* **2021**, *21*, 9838−9844.
(14) Takeyama, K.; Moriya, R.; Okazaki, S.; Zhang, Y. J.; Masubuchi, S.; Watanabe, K.; Taniguchi, T.; Sasagawa, T.; Machida, T. Resonant Tunneling Due to van der Waals Quantum-Well States of Few-Layer WSe_2 in WSe_2/h-BN/p^+-MoS_2 Junction. *Nano Lett.* **2021**, *21*, 3929−3934.
(15) Lv, L.; Yu, J.; Hu, M.; Yin, S. M.; Zhuge, F. W.; Ma, Y.; Zhai, T. Y. Design and tailoring of two-dimensional Schottky, PN and tunnelling junctions for electronics and optoelectronics. *Nanoscale* **2021**, *13*, 6713−6751.
(16) Zou, Z. X.; Li, D.; Liang, J. W.; Zhang, X. H.; Liu, H. W.; Zhu, C. G.; Yang, X.; Li, L. H.; Zheng, B. Y.; Sun, X. X.; Zeng, Z. X. S.; Yi, J. L.; Zhuang, X. J.; Wang, X.; Pan, A. L. Epitaxial synthesis of ultrathin beta-In2Se_3/MoS_2 heterostructures with high visible/near-infrared photoresponse. *Nanoscale* **2020**, *12*, 6480−6488.
(17) Sun, Z.; Martinez, A.; Wang, F. Optical modulators with 2D layered materials. *Nat. Photonics* **2016**, *10*, 227−238.
(18) Wu, J.; Lu, Y.; Feng, S.; Wu, Z.; Lin, S.; Hao, Z.; Yao, T.; Li, X.; Zhu, H.; Lin, S. The Interaction between Quantum Dots and Graphene: The Applications in Graphene-Based Solar Cells and Photodetectors. *Adv. Funct. Mater.* **2018**, *28*, 1804712.
(19) Mišeikis, V.; Marconi, S.; Giambra, M. A.; Montanaro, A.; Martini, L.; Fabbri, F.; Pezzini, S.; Piccinini, G.; Forti, S.; Terrés, B.; Goykhman, I.; Hamidouche, L.; Legagneux, P.; Sorianello, V.; Ferrari, A. C.; Koppens, F. H. L.; Romagnoli, M.; Coletti, C. Ultrafast, Zero-Bias, Graphene Photodetectors with Polymeric Gate Dielectric on Passive Photonic Waveguides. *ACS Nano* **2020**, *14*, 11190−11204.
(20) Ma, Y.; Chang, Y.; Dong, B.; Wei, J.; Liu, W.; Lee, C. Heterogeneously Integrated Graphene/Silicon/Halide Waveguide Photodetectors toward Chip-Scale Zero-Bias Long-Wave Infrared Spectroscopic Sensing. *ACS Nano* **2021**, *15*, 10084−10094.
(21) Gan, X.; Shiue, R.-J.; Gao, Y.; Meric, I.; Heinz, T. F.; Shepard, K.; Hone, J.; Assefa, S.; Englund, D. Chip-integrated ultrafast graphene photodetector with high responsivity. *Nat. Photonics* **2013**, *7*, 883−887.
(22) Wang, X.; Cheng, Z.; Xu, K.; Tsang, H. K.; Xu, J.-B. High-responsivity graphene/silicon-heterostructure waveguide photodetectors. *Nat. Photonics* **2013**, *7*, 888−891.
(23) Shiue, R.-J.; Gao, Y.; Wang, Y.; Peng, C.; Robertson, A. D.; Efetov, D. K.; Assefa, S.; Koppens, F. H.; Hone, J.; Englund, D. High-responsivity graphene-boron nitride photodetector and autocorrelator in a silicon photonic integrated circuit. *Nano Lett.* **2015**, *15*, 7288−7293.
(24) Goykhman, I.; Sassi, U.; Desiatov, B.; Mazurski, N.; Milana, S.; De Fazio, D.; Eiden, A.; Khurgin, J.; Shappir, J.; Levy, U.; et al. On-chip integrated, silicon-graphene plasmonic Schottky photodetector with high responsivity and avalanche photogain. *Nano Lett.* **2016**, *16*, 3005−3013.
(25) Wu, J.; Wei, M.; Mu, J.; Ma, H.; Zhong, C.; Ye, Y.; Sun, C.; Tang, B.; Wang, L.; Li, J.; Xu, X.; Liu, B.; Li, L.; Lin, H. High-Performance Waveguide-Integrated Bi_2O_2Se Photodetector for Si Photonic Integrated Circuits. *ACS Nano* **2021**, *15*, 15982−15991.
(26) Flöry, N.; Ma, P.; Salamin, Y.; Emboras, A.; Taniguchi, T.; Watanabe, K.; Leuthold, J.; Novotny, L. Waveguide-integrated van der Waals heterostructure photodetector at telecom wavelengths with high speed and high responsivity. *Nat. Nanotechnol.* **2020**, *15*, 118−124.
(27) Youngblood, N.; Chen, C.; Koester, S. J.; Li, M. Waveguide-integrated black phosphorus photodetector with high responsivity and low dark current. *Nat. Photonics* **2015**, *9*, 247−252.
(28) Yin, Y.; Cao, R.; Guo, J.; Liu, C.; Li, J.; Feng, X.; Wang, H.; Du, W.; Qadir, A.; Zhang, H.; Ma, Y.; Gao, S.; Xu, Y.; Shi, Y.; Tong, L.; Dai, D. High-Speed and High-Responsivity Hybrid Silicon/Black-Phosphorus Waveguide Photodetectors at 2 μm. *Laser Photonics Rev.* **2019**, *13*, 1900032.
(29) Cheng, P. K.; Tang, C. Y.; Ahmed, S.; Qiao, J. P.; Zeng, L. H.; Tsang, Y. H. Utilization of group 10 2D TMDs-$PdSe_2$ as a nonlinear optical material for obtaining switchable laser pulse generation modes. *Nanotechnology* **2021**, *32*, 055201.
(30) Luo, L. B.; Wang, D.; Xie, C.; Hu, J. G.; Zhao, X. Y.; Liang, F. X. $PdSe_2$ Multilayer on Germanium Nanocones Array with Light Trapping Effect for Sensitive Infrared Photodetector and Image Sensing Application. *Adv. Funct. Mater.* **2019**, *29*, 1900849.
(31) Sun, J.; Shi, H.; Siegrist, T.; Singh, D. J. Electronic, transport, and optical properties of bulk and mono-layer $PdSe_2$. *Appl. Phys. Lett.* **2015**, *107*, 153902.
(32) Oyedele, A. D.; Yang, S.; Liang, L.; Puretzky, A. A.; Wang, K.; Zhang, J.; Yu, P.; Pudasaini, P. R.; Ghosh, A. W.; Liu, Z.; Rouleau, C. M.; Sumpter, B. G.; Chisholm, M. F.; Zhou, W.; Rack, P. D.; Geohegan, D. B.; Xiao, K. $PdSe_2$: Pentagonal Two-Dimensional Layers with High Air Stability for Electronics. *J. Am. Chem. Soc.* **2017**, *139*, 14090−14097.
(33) Liang, F.-X.; Zhao, X.-Y.; Jiang, J.-J.; Hu, J.-G.; Xie, W.-Q.; Lv, J.; Zhang, Z.-X.; Wu, D.; Luo, L.-B. Light Confinement Effect Induced Highly Sensitive, Self-Driven Near-Infrared Photodetector and Image Sensor Based on Multilayer $PdSe_2$/Pyramid Si Heterojunction. *Small* **2019**, *15*, 1903831.
(34) Zeng, L.-H.; Wu, D.; Lin, S.-H.; Xie, C.; Yuan, H.-Y.; Lu, W.; Lau, S. P.; Chai, Y.; Luo, L.-B.; Li, Z.-J.; Tsang, Y. H. Controlled Synthesis of 2D Palladium Diselenide for Sensitive Photodetector Applications. *Adv. Funct. Mater.* **2019**, *29*, 1806878.
(35) Wei, M.; Lian, J.; Zhang, Y.; Wang, C.; Wang, Y.; Xu, Z. Layer-dependent optical and dielectric properties of centimeter-scale $PdSe_2$ films grown by chemical vapor deposition. *NPJ. 2D Mater. Appl.* **2022**, *6*, 1−8.
(36) Liang, Q. J.; Wang, Q. X.; Zhang, Q.; Wei, J. X.; Lim, S. X. D.; Zhu, R.; Hu, J. X.; Wei, W.; Lee, C.; Sow, C.; Zhang, W. J.; Wee, A. T. S. High-Performance, Room Temperature, Ultra-Broadband Photodetectors Based on Air-Stable $PdSe_2$. *Adv. Mater.* **2019**, *31*, 1807609.
(37) Long, M.; Wang, Y.; Wang, P.; Zhou, X.; Xia, H.; Luo, C.; Huang, S.; Zhang, G.; Yan, H.; Fan, Z.; Wu, X.; Chen, X.; Lu, W.; Hu, W. Palladium Diselenide Long-Wavelength Infrared Photodetector with High Sensitivity and Stability. *ACS Nano* **2019**, *13*, 2511−2519.
(38) Ahmad, W.; Liu, J.; Jiang, J.; Hao, Q.; Wu, D.; Ke, Y.; Gan, H.; Laxmi, V.; Ouyang, Z.; Ouyang, F.; Wang, Z.; Liu, F.; Qi, D.; Zhang, W. Strong Interlayer Transition in Few-Layer InSe/$PdSe_2$ van der Waals Heterostructure for Near-Infrared Photodetection. *Adv. Funct. Mater.* **2021**, *31*, 2104143.
(39) Ye, C.; Yang, Z.; Dong, J.; Huang, Y.; Song, M.; Sa, B.; Zheng, J.; Zhan, H. Layer-Tunable Nonlinear Optical Characteristics and Photocarrier Dynamics of 2D $PdSe_2$ in Broadband Spectra. *Small* **2021**, *17*, 2103938.
(40) Sun, D.; Wu, Z.-K.; Divin, C.; Li, X.; Berger, C.; de Heer, W. A.; First, P. N.; Norris, T. B. Ultrafast relaxation of excited Dirac fermions in epitaxial graphene using optical differential transmission spectroscopy. *Phys. Rev. Lett.* **2008**, *101*, 157402.
(41) Long, M.; Wang, P.; Fang, H.; Hu, W. Progress, Challenges, and Opportunities for 2D Material Based Photodetectors. *Adv. Funct. Mater.* **2019**, *29*, 1803807.
(42) Zhang, G.; Amani, M.; Chaturvedi, A.; Tan, C.; Bullock, J.; Song, X.; Kim, H.; Lien, D.-H.; Scott, M. C.; Zhang, H.; Javey, A. Optical and electrical properties of two-dimensional palladium diselenide. *Appl. Phys. Lett.* **2019**, *114*, 253102.
(43) Liu, Y.; Guo, J.; Zhu, E.; Liao, L.; Lee, S.-J.; Ding, M.; Shakir, I.; Gambin, V.; Huang, Y.; Duan, X. Approaching the Schottky-Mott limit in van der Waals metal-semiconductor junctions. *Nature* **2018**, *557*, 696−700.
(44) Xie, C.; Jiang, S.; Gao, Y.; Hong, M.; Pan, S.; Zhao, J.; Zhang, Y. Giant Thickness-Tunable Bandgap and Robust Air Stability of 2D Palladium Diselenide. *Small* **2020**, *16*, 2000754.
(45) Li, P.; Zhang, J.; Zhu, C.; Shen, W.; Hu, C.; Fu, W.; Yan, L.; Zhou, L.; Zheng, L.; Lei, H.; Liu, Z.; Zhao, W.; Gao, P.; Yu, P.; Yang, G. Penta-PdPSe: A New 2D Pentagonal Material with Highly In-Plane Optical, Electronic, and Optoelectronic Anisotropy. *Adv. Mater.* **2021**, *33*, 2102541.

https://doi.org/10.1021/acs.nanolett.2c02099
Nano Lett. XXXX, XXX, XXX−XXX

(46) Shiue, R.-J.; Gao, Y.; Wang, Y.; Peng, C.; Robertson, A. D.; Efetov, D. K.; Assefa, S.; Koppens, F. H. L.; Hone, J.; Englund, D. High-Responsivity Graphene-Boron Nitride Photodetector and Autocorrelator in a Silicon Photonic Integrated Circuit. *Nano Lett.* **2015**, *15*, 7288−7293.
(47) Schuler, S.; Schall, D.; Neumaier, D.; Dobusch, L.; Bethge, O.; Schwarz, B.; Krall, M.; Mueller, T. Controlled Generation of a p-n Junction in a Waveguide Integrated Graphene Photodetector. *Nano Lett.* **2016**, *16*, 7107−7112.
(48) Ma, P.; Flöry, N.; Salamin, Y.; Baeuerle, B.; Emboras, A.; Josten, A.; Taniguchi, T.; Watanabe, K.; Novotny, L.; Leuthold, J. Fast $MoTe_2$ Waveguide Photodetector with High Sensitivity at Telecommunication Wavelengths. *ACS Photonics* **2018**, *5*, 1846−1852.
(49) Pi, L.; Hu, C.; Shen, W.; Li, L.; Luo, P.; Hu, X.; Chen, P.; Li, D.; Li, Z.; Zhou, X.; et al. Highly In-Plane Anisotropic 2D $PdSe_2$ for Polarized Photodetection with Orientation Selectivity. *Adv. Funct. Mater.* **2021**, *31*, 2006774.
(50) Wu, D.; Jia, C.; Shi, F.; Zeng, L.; Lin, P.; Dong, L.; Shi, Z.; Tian, Y.; Li, X.; Jie, J. Mixed-dimensional $PdSe_2$/SiNWA heterostructure based photovoltaic detectors for self-driven, broadband photodetection, infrared imaging and humidity sensing. *J. Mater. Chem. A* **2020**, *8*, 3632−3642.
(51) Lopez-Sanchez, O.; Lembke, D.; Kayci, M.; Radenovic, A.; Kis, A. Ultrasensitive photodetectors based on monolayer MoS_2. *Nat. Nanotechnol.* **2013**, *8*, 497−501.
(52) Youngblood, N.; Anugrah, Y.; Ma, R.; Koester, S. J.; Li, M. Multifunctional graphene optical modulator and photodetector integrated on silicon waveguides. *Nano Lett.* **2014**, *14*, 2741−2746.
(53) Chen, T.; Bobbert, P. A.; van der Wiel, W. G. 1/f Noise and Machine Intelligence in a Nonlinear Dopant Atom Network. *Small Science* **2021**, *1*, 2000014.
(54) Balandin, A. A. Low-frequency 1/f noise in graphene devices. *Nat. Nanotechnol.* **2013**, *8*, 549−555.
(55) Wolf, D. *Noise in Physical Systems: Proceedings of the Fifth International Conference on Noise, Bad Nauheim, Fed. Rep. of Germany, March 13−16, 1978*; Springer Science & Business Media: 2013; Vol. 2.
(56) Chow, W. L.; Yu, P.; Liu, F.; Hong, J.; Wang, X.; Zeng, Q.; Hsu, C.-H.; Zhu, C.; Zhou, J.; Wang, X.; Xia, J.; Yan, J.; Chen, Y.; Wu, D.; Yu, T.; Shen, Z.; Lin, H.; Jin, C.; Tay, B. K.; Liu, Z. High Mobility 2D Palladium Diselenide Field-Effect Transistors with Tunable Ambipolar Characteristics. *Adv. Mater.* **2017**, *29*, 1602969.
(57) Ma, Y.; Dong, B.; Wei, J.; Chang, Y.; Huang, L.; Ang, K. W.; Lee, C. High-Responsivity Mid-Infrared Black Phosphorus Slow Light Waveguide Photodetector. *Adv. Opt. Mater.* **2020**, *8*, 2000337.
(58) Tian, R.; Gu, L.; Ji, Y.; Li, C.; Chen, Y.; Hu, S.; Li, Z.; Gan, X.; Zhao, J. Black Phosphorus Photodetector Enhanced by a Planar Photonic Crystal Cavity. *ACS Photonics* **2021**, *8*, 3104−3110.
(59) Bie, Y.-Q.; Grosso, G.; Heuck, M.; Furchi, M. M.; Cao, Y.; Zheng, J.; Bunandar, D.; Navarro-Moratalla, E.; Zhou, L.; Efetov, D. K.; et al. A $MoTe_2$-based light-emitting diode and photodetector for silicon photonic integrated circuits. *Nat. Nanotechnol.* **2017**, *12*, 1124−1129.
(60) Li, G.; Yin, S.; Tan, C.; Chen, L.; Yu, M.; Li, L.; Yan, F. Fast Photothermoelectric Response in CVD-Grown $PdSe_2$ Photodetectors with In-Plane Anisotropy. *Adv. Funct. Mater.* **2021**, *31*, 2104787.
(61) Wu, D.; Guo, J.; Du, J.; Xia, C.; Zeng, L.; Tian, Y.; Shi, Z.; Tian, Y.; Li, X. J.; Tsang, Y. H.; et al. Highly polarization-sensitive, broadband, self-powered photodetector based on graphene/$PdSe_2$/germanium heterojunction. *ACS Nano* **2019**, *13*, 9907−9917.
(62) Dong, Z.; Yu, W.; Zhang, L.; Mu, H.; Xie, L.; Li, J.; Zhang, Y.; Huang, L.; He, X.; Wang, L.; Lin, S.; Zhang, K. Highly Efficient, Ultrabroad $PdSe_2$ Phototransistors from Visible to Terahertz Driven by Mutiphysical Mechanism. *ACS Nano* **2021**, *15*, 20403−20413.
(63) Maiti, R.; Patil, C.; Saadi, M. A. S. R.; Xie, T.; Azadani, J. G.; Uluutku, B.; Amin, R.; Briggs, A. F.; Miscuglio, M.; Van Thourhout, D.; Solares, S. D.; Low, T.; Agarwal, R.; Bank, S. R.; Sorger, V. J. Strain-engineered high-responsivity $MoTe_2$ photodetector for silicon photonic integrated circuits. *Nat. Photonics* **2020**, *14*, 578−584.
(64) Zhong, J.; Wu, B.; Madoune, Y.; Wang, Y.; Liu, Z.; Liu, Y. $PdSe_2$/$MoSe_2$ vertical heterojunction for self-powered photodetector with high performance. *Nano Research* **2022**, *15*, 2489−2496.

https://doi.org/10.1021/acs.nanolett.2c02099
Nano Lett. XXXX, XXX, XXX−XXX